Point-to-point responses

We appreciate the reviewers for their valuable and constructive comments, which are very helpful for the improvement of the manuscript. We have revised the manuscript carefully according to the reviewers' comments. We have addressed the reviewers' comments on a point-to-point basis as below for consideration, where the reviewers' comments are cited in ***black****, and the responses are in* ***blue****.*

Review for the Manuscript "Vertical Structure and Seasonal Evolution of Atmospheric Oxidizing Capacity across Urban and Rural Regions: Observational Constraints from OH Radical Production Pathways" by Zou et al. for EGUSPHERE / ACP.

The manuscript by Zou et al. deals with a determination of the main pathways for OH production over a urban and a remote location in China in the lower troposphere. For that purpose, DOAS measurements for the main components for potential OH production have been obtained and their temporal evolution is analysed. Afterwards, with the help of a photolysis rate model, the respective OH production pathways and efficiencies are determined and the relative importance of the individual branches of OH production are analysed.

Overall, the manuscript deals with an interesting topic, but in conclusion it does not become obvious how and whether these findings can be generalised or a subject to the local conditions. Furthermore, the methodology does not fully become clear, how the conclusion can be reached (see details below). I do not agree with some of the motivation and concluding remarks, i.e., that these processes and new findings must be considered in chemistry transport models, as this is exactly done in ALL chemistry transport models, namely the inclusion of multiple reaction pathways and their relative importance is considered by treating the chemistry by a set of chemical differential equations, at least as long as all three photolysis rates are included.

The general view and results presented in 3.4 - which are the main findings of the study according to title and abstract - are fine from my point of view.

Overall, there are still many flaws and weaknesses in this manuscript, which must be revised with major changes before a publication can be re-considered.

Major comments:

1) You use measurements under 11 elevation levels. It is not clear to me, how from this you can get vertical profiles with detailed information on a much higher resolution as shown in Fig.2 where you have almost 50 to 100 data points in the vertical. Of course, you can consider a vertical profile (a-priori) with multiple levels, but your different elevation angles provide you with more limited vertical independent information. You

only get 11 different SCDs from which you have to generate a vertical profile.

So you have to clarify, how you obtain this high vertical resolution, which might be crucial for all subsequent analysis! If this is part of VLIDORT and your optical estimation method, elaborate this a bit better!

***Re*:** Thank you for your comments.

(1) First, it should be clarified that the number of observation elevation angles is not linearly proportional to the vertical resolution of the gas vertical profiles. Our instrument collects scattered sunlight and inherently possesses a finite field of view (FOV). Consequently, employing a spatially overly dense set of elevation angles would lead to an overlap of the incident light paths, thereby compromising the accuracy of the retrieved measurement information. Currently, the vertical resolution achieved by our system represents a leading standard on a global scale.

(2) deriving high-resolution vertical profiles from observations at a limited number of 11 discrete elevation angles is indeed achieved by relying on the OEM combined with the forward simulation of a pseudo-spherical vector discrete ordinate radiative transfer model, rather than a direct analytical transformation. This process has established a complete theoretical foundation in Rodgers' classic work "Inverse Methods for Atmospheric Sounding: Theory and Practice" and has been widely standardized within the MAX-DOAS community (Frieß et al., 2006a, 2019; Rodgers, 2000b). The detailed mathematical and physical mechanisms are as follows:

① The DSCDs measured by MAX-DOAS at 11 different elevation angles are essentially integrals of the target gas concentration along the optical path in the atmosphere. Due to atmospheric scattering (particularly aerosol Mie scattering and Rayleigh scattering), the optical path lengths and weighting functions differ significantly across elevation angles: the optical paths at low elevation angles (e.g., 1°–2°) mainly traverse the near-surface boundary layer and are extremely sensitive to near-surface concentrations; whereas the optical paths at high elevation angles (e.g., 30°, 90°) reflect more of the background concentrations at high altitudes and in the free troposphere. These 11 elevation angles of DSCDs constitute a finite-dimensional observation vector y.

② However, 11 observation values obviously cannot be directly analytically resolved into 40 independent concentration layers with a vertical resolution of 0.1 km in the 0–4 km range. Within the OEM framework (refer to Rodgers(2000)), we discretize the atmosphere into multi-layer grids and construct a priori state vector x_a. The core of the retrieval lies in minimizing the cost function χ^2, which simultaneously constrains the observation fitting residuals and the deviations from the a priori. In this process, the VLIDORT model (Frieß et al., 2006a) not only forward-simulates the DSCDs at each elevation angle, more critically, provides the Jacobian matrix (or weighting function matrix K),

which is the partial derivative $\partial y/\partial x$ of the DSCD at each elevation angle with respect to the concentration change in each altitude layer. This reflects the contribution weight of different altitude layers to the observations.

③ In OEM retrieval, although the grid is finely divided (presenting a high visual resolution), the actual independent information content is limited by the DOF. For the MAX-DOAS setup in this paper, the DOF is typically between 2.5 and 4.5 (Frieß et al., 2006a; Wang et al., 2020; Xing et al., 2017, 2019). This means that the retrieved high-resolution vertical profiles are actually the weighted smoothing of the true atmospheric state and the a priori profile, which involves a strong covariance smoothing effect between adjacent altitude layers. The a priori profile is typically assumed to decay exponentially with altitude (reflecting the general distribution pattern of boundary layer pollutants), and the a priori covariance matrix Sa sets the spatial scale of vertical correlation. Therefore, the high vertical resolution displayed in Figure 2 contains not only the independent information brought by the observations but also the interpolation and smoothing information from the OEM algorithm under a priori constraints.

(3) In summary, the high vertical resolution is a mathematical expression of the OEM algorithm in solving the cost function on a discretized grid, rather than purely independent observation points. This method has been widely validated and accepted in the MAX-DOAS field (Wang et al., 2020; Xing et al., 2019, 2023). We will supplement the details of the OEM retrieval theory in Section 2.2 of the revised manuscript, particularly specifying the limitation of the DOF and the constraining role of a priori information on the vertical shape of the profile, to dispel the reviewer's concerns.

2) For the TUV calculations, you use AOD from your own retrievals. How is the AOD vertically distributed? If this is the result shown in Fig.S5, where does the high vertical resolution originate from? How does the data look like at the other station? How much of this information depends on the initial profile assumption? Can elevated aerosol layers above the PBL be measured or retrieved? Why is there such a strong decline in aerosol load after 3pm LT?

And do the O_3 values for TUV include the DOAS measurements or is it assumed that all O_3 is located above, i.e., mainly the stratospheric column with the TROPOMI satellite data?

***Re*:** Thank you for your comments.

(1) It should be clarified that the aerosol optical depth (AOD) is a column-integrated quantity without vertical distribution, whereas the aerosol extinction profile characterizes the vertical variability of aerosols. The vertical integral of the aerosol extinction coefficient yields the AOD.

(2) Figure S5 (referred to as Figure R1-1 in this response) displays the aerosol extinction vertical profile

rather than the vertical distribution of AOD. The high vertical resolution of the aerosol extinction profile, consistent with the explanation provided in our response to Comment 1), is achieved through the inversion algorithm. During the retrieval process of trace gas vertical profiles, the aerosol vertical profile is first retrieved and subsequently employed as a priori information to constrain the retrieval of the trace gas vertical profiles.

(3) The aerosol extinction vertical profiles exhibit distinct variabilities across different observation sites. Jiao et al., (2025) comprehensively presented the diurnal variations of the overall mean aerosol extinction vertical profiles observed by our research group across 32 sites from 2019 to 2023 (Figure R1-2).

(4) The detailed inversion procedure for the aerosol extinction vertical profile is as follows: The aerosol vertical distribution is retrieved utilizing the O_4 absorption at the 360 nm and 477 nm wavebands (Xing et al., 2019; Zou et al., 2026). Given that the O_4 vertical concentration profile is known a priori (decreasing exponentially with altitude), the DSCDs of O_4 are highly sensitive to aerosol extinction. The OEM algorithm is utilized to invert the O_4 profile, thereby deriving the aerosol extinction profile. Admittedly, due to the limited information content inherent to MAX-DOAS observations, the retrieved aerosol profiles are inevitably influenced by the a priori assumption (exponential decay), particularly in high-altitude regions characterized by a poor signal-to-noise ratio. Nevertheless, the observational information dominates, ensuring that the retrieved aerosol layer structures are fundamentally reliable.

(5) Our instrument is capable of detecting aerosol extinction above the PBL, with an effective probing altitude range of 0–4 km. In the field of DOAS probing and inversion, our research group currently represents a leading team globally.

(6) We investigated the temporal variations in near-surface $PM_{2.5}$ concentrations measured at the nearest national monitoring station (2.23 km away from the AHU site) during the same time period (Figure R1-3). It can be clearly observed that the $PM_{2.5}$ concentration exhibits a dramatic decrease after 15:00 local time, which overall corresponds to the temporal trend of AOD. This phenomenon is predominantly driven by the dynamical processes within the boundary layer: solar heating elevates the PBL to its daily maximum height (PBL information is shown in Figure R1-4), and enhanced turbulence disperses the pollutants accumulated during the morning into a deeper air column, leading to a reduction in near-surface $PM_{2.5}$ concentrations. Simultaneously, the afternoon decrease in relative humidity weakens the extinction of hygroscopic aerosols, which, compounded by the intensification of local circulations facilitating the horizontal transport of pollutants, collectively drives the decline in AOD. This mechanism is corroborated by multi-city observations: the minimum $PM_{2.5}$ values in the afternoon at Chinese sites correspond well with the PBL peak (Guo et al., 2017), and a significant negative

correlation between PBL height and $PM_{2.5}$ concentrations has also been documented in cities such as Beijing and Shenzhen (Fu et al., 2020).

(7) Regarding the input of O_3 in the TUV model: When the TUV model calculates photolysis rates, the absorption of ultraviolet radiation is partitioned into stratospheric and tropospheric components. For the background absorption by stratospheric O_3, we utilized the daily total column O_3 product from the TROPOMI satellite (260–280 DU). Conversely, for tropospheric O_3—particularly when calculating the $J(O(^1D))$ photolysis rate for O_3 producing $O(^1D)$—high concentrations of near-surface O_3 enhance the local absorption of photons. Therefore, in the lower atmospheric module of the TUV model, we directly input the O_3 vertical profiles retrieved by MAX-DOAS. This approach ensures that the calculation of photolysis frequencies accounts for both the background UV shielding effect of the stratosphere and precisely incorporates the local radiative feedback effects of tropospheric O_3 (Liao et al., 2024; Wang et al., 2020).

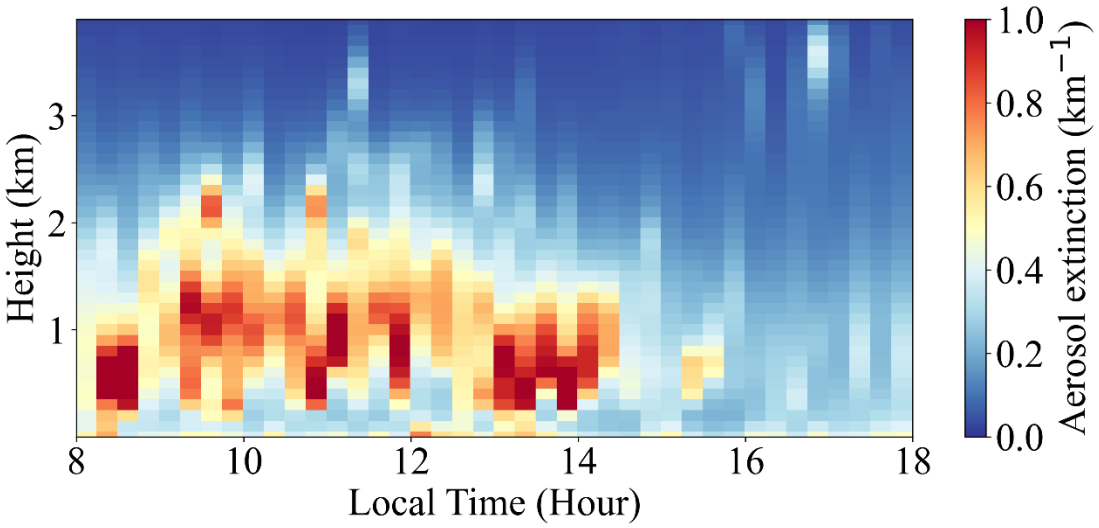

Figure R1-1. Vertical aerosol extinction profiles for summer at AHU.

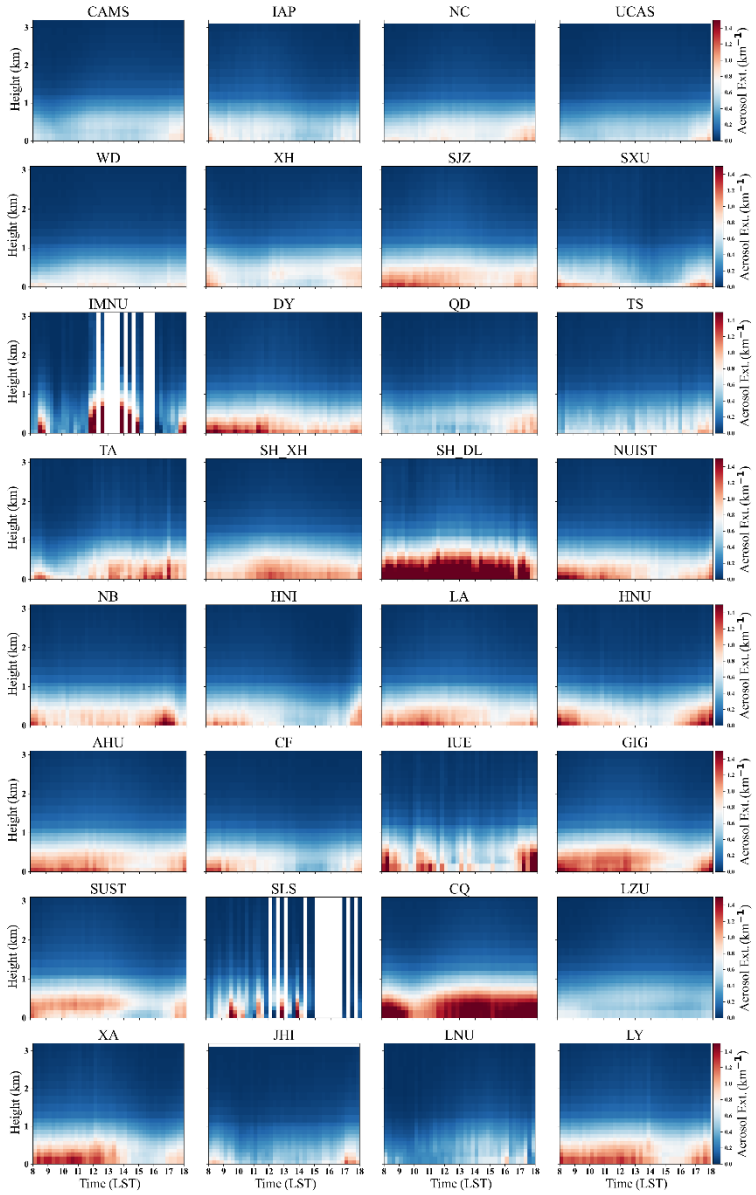

Figure R1-2. Diurnal variation of the total averaged aerosol extinction vertical profiles during 2019-2023(Jiao et al., 2025)

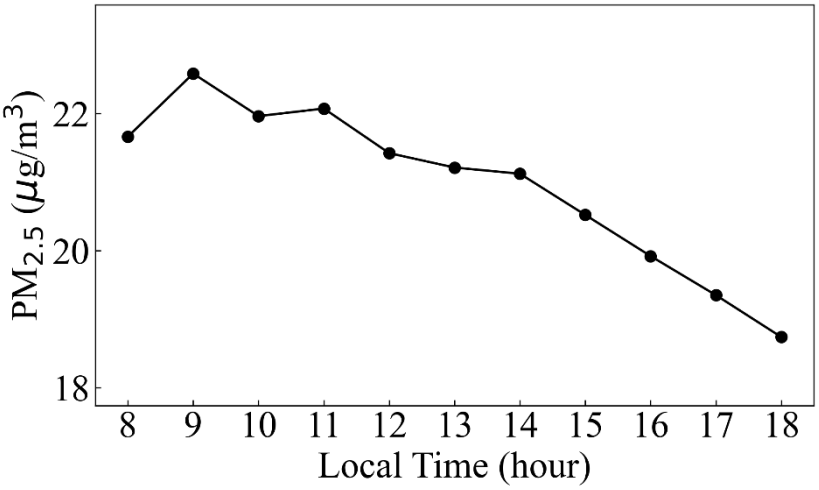

Figure R1-3. Diurnal variations of $PM_{2.5}$ at the state-controlled monitoring site nearest to the AHU station during summer.

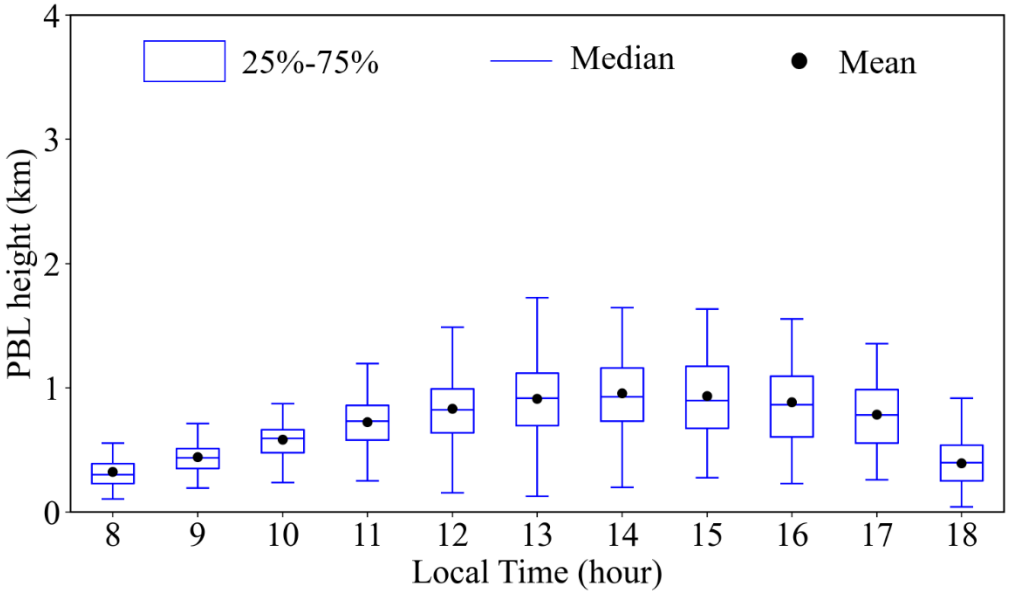

Figure R1-4. PBL height at AHU in Summer

3) What is the detection limit and accuracy level for the DOAS measurements? The HONO values are often < 100 pptv which could already be close to detection? Into which uncertainty for mixing ratios do the retrieval or fit uncertainties propagate, especially including the vertical distribution (point 1)?

This becomes even more important, when the direct emissions of HONO are excluded by your selected correction mechanism. The correlation for this correction with a value of R=0.75 is not very strong. Nevertheless, the remaining (secondary) HONO is < 50 pptv. You should discuss whether this quantity can reliably be determined from your measurements! Furthermore, as OH production from HONO originates from the photolysis of HONO (independent whether HONO is primarily emitted or secondarily formed) you should justify the restriction to secondary HONO only, even though all HONO can photolyse and produce OH.

***Re*:** Thank you for your comments.

(1) Detection limit and accuracy: The retrieval accuracy of HONO by MAX-DOAS highly depends on the spectral fitting quality and the optical path length. In this study, we strictly adopted the fitting window and parameters recommended by the CINDI-2 international intercomparison experiment (Wang et al., 2020). Under strong light conditions, combined with strict RMS filtering ($<1\times10^{-3}$), the DSCD detection limit of HONO is typically around 1×10^{15} molecules/cm^2. Considering that the optical path length at low elevation angles (e.g., 1°–2°) can reach 10–20 km, according to the Beer-Lambert law, this is equivalent to a volume mixing ratio detection limit as low as 50–100 pptv within the near-surface layer of a few meters to tens of meters. Previous extensive HONO observations based on MAX-DOAS (Xing et al., 2024a) have demonstrated that even under clean background conditions or after subtracting source contributions where concentrations are low, MAX-DOAS can still provide reliable HONO

column densities. The total HONO retrieval error evaluated in Section S1 of the manuscript is 16% (primarily caused by smoothing errors). Within the allowable error range, secondary HONO column densities at the 50 pptv level can be effectively detected.

(2) Retrieval error and uncertainty: We have elaborated on this in detail in the supplemental material (Section S1, Error analysis), and the specific contents are detailed as follows:

We evaluated uncertainties in the retrieved profile products by analyzing the vertical column densities (VCDs) of trace gases (HONO, HCHO and O_3) and AOD. The main sources of uncertainty considered here were smoothing and noise errors, absorption cross-section uncertainties, errors arising from the temperature dependence of absorption cross-sections, algorithmic errors, and uncertainties related to aerosol retrievals. Each component is described below.

Smoothing and noise errors ($\sigma_{smooth\ noise}$): Smoothing error (Ss) reflects the limited vertical resolution of the inversion and was calculated using Eq. S1. Noise error (Sn) arises from DOAS fitting uncertainty, primarily driven by measurement noise. The uncertainty in the retrieved state vector ($\widehat{S}$) was treated as the combined contribution of these two independent sources and quantified using Eq. S2 (Frieß et al., 2006b). In this study, the total smoothing and noise uncertainty was derived from the mean profile retrieval uncertainty.

$$S_s = (AK - 1)S_a(AK - 1)^T \tag{S1}$$

$$\widehat{S} = (K^T S_a^{-1} K + S_\varepsilon^{-1})^{-1} \tag{S2}$$

Here, AK denotes the averaging kernel matrix, which describes the sensitivity of the retrieved state to the true atmospheric state. S_a and S_ε are the covariance matrices of the a priori constraints and measurements, respectively. K is the weighting-function Jacobian matrix, representing the sensitivity of the measurements to perturbations in the state vector.

Absorption cross-section uncertainties ($\sigma_{cross\ section}$): Uncertainty in the absorption cross-sections is an inherent source of retrieval error. Previous studies have shown that the resulting uncertainties propagated to VCDs and vertical profiles are comparable to the original cross-section uncertainties (Friedrich et al., 2019; Song et al., 2023). We therefore adopted the reported intrinsic uncertainties of the cross-sections directly. The uncertainties for O_4, HONO, HCHO and O_3 were 4%, 3%, 5% and 3%, respectively (Orphal and Chance, 2003; Paur and Bass, 1985; R and R, 2013; Vandaele et al., 1998).

Temperature-dependent absorption cross-section uncertainties ($\sigma_{temperature}$): Trace-gas absorption cross-sections vary with temperature and therefore introduce an additional source of uncertainty. This systematic error was estimated by calculating the change in cross-section magnitude per kelvin between two reference temperatures and multiplying it by the maximum temperature variation during the campaign. The measurement period (1 March to 31 August 2023) spanned spring and summer, for which a maximum temperature difference of 30 K was assumed. The resulting uncertainties for O_4,

HONO, HCHO and O_3 were approximately 10%, 2%, 6% and 13%, respectively.

Algorithmic error ($\sigma_{algorithm}$): This term represents the mismatch between the measured differential slant column density (DSCDs; y) and the simulated value ($F(x,b)$). As expressed in Eq. S3, this discrepancy may arise from imperfections in the forward model, inappropriate specification of parameter b, and errors independent of forward-model parameters, such as detector noise (Wang et al., 2017).

$$\sigma_{algorithm} = y - F(x,b) \tag{S3}$$

Aerosol-retrieval-related uncertainties ($\sigma_{aerosol}$): The aerosol vertical profile is a key input to trace-gas profile retrieval and strongly influences the inversion results. Uncertainties in the retrieved aerosol extinction profile propagate directly into the trace-gas VCDs. This contribution was quantified using Eq. S4.

$$\sigma_{aerosol} = \sqrt{(\sigma_{smooth\ noise})^2 + (\sigma_{cross\ section})^2 + (\sigma_{temperature})^2 + (\sigma_{algorithm})^2} \tag{S4}$$

The total uncertainty for each trace gas was then derived by Gaussian error propagation, as given in Eq. S5.

$$\sigma_{total} = \sqrt{(\sigma_{smooth\ noise})^2 + (\sigma_{cross\ section})^2 + (\sigma_{temperature})^2 + (\sigma_{aerosol})^2 + (\sigma_{algorithm})^2} \tag{S5}$$

Using the framework described above, the estimated uncertainties for trace gases (HONO, HCHO and O_3) and AOD are summarized in Table R1-1.

Table R1-1. Mean uncertainty estimates for trace gases and AOD (%)

		VCD		
	AOD	HONO	HCHO	O_3
$\sigma_{smooth\ noise}$	5	16	27	8
$\sigma_{cross\ section}$	4	2	5	3
$\sigma_{temperature}$	10	2	6	13
$\sigma_{algorithm}$	8	11	11	5
$\sigma_{aerosol}$	/	14	14	14
Total	14	24	33	22

(3) Reliability of secondary HONO quantification: The reviewer acutely pointed out “whether the residual secondary HONO <50 pptv (0.045 ppb) is reliable.” It needs to be clarified that the HONO/NOx slope method (R=0.75) is used to subtract direct emissions, which has been validated as effective in tunnel and urban studies by (Kramer et al., 2020) (an R of 0.6–0.8 being the norm). The slope of 0.79%±0.54% is consistent with urban values in the literature (0.5–1.5%) (Li et al., 2021).

(4) Validation of HONO data accuracy: In our previous studies, our research group conducted rigorous accuracy validation for the instrumentally measured HONO. It should be noted that the instrument utilized in this study possesses identical instrumental parameters and performance characteristics to those employed in the earlier studies. The validation of HONO data accuracy is presented in Figure R1-5 (Xing et al., 2024c).

(5) Clarification of photolysis calculation logic: The reviewer emphasized that "all HONO photolyzes to produce OH, so it should not be limited to secondary sources." We completely agree with this chemical fact! When calculating in Section 3.4 of the manuscript, the total observed HONO concentration (including direct emissions and secondary sources) was used, rather than the subtracted secondary fraction. There is a misunderstanding here that needs clarification. We subtracted directly emitted HONO in the text solely for use in calculating the heterogeneous conversion rate $C_{(HONO)}$ in Section 3.2, not to exclude it when calculating P(OH) in Section 3.4. The definition of $C_{(HONO)}$ is the rate of NO_2 conversion to HONO; if traffic-directly-emitted HONO were included, the true conversion capacity of heterogeneous chemistry would be severely overestimated. When calculating the OH radical production rate $P(OH)_{HONO}$ in Section 3.4, the [HONO] used in Equation (3) is the measured total HONO concentration including all sources. Whether from direct emissions or secondary generation, HONO will photolyze to produce OH under illumination. We completely agree with your viewpoint and have already reflected this in the calculations. We will explicitly state this in the revised manuscript to avoid ambiguity.

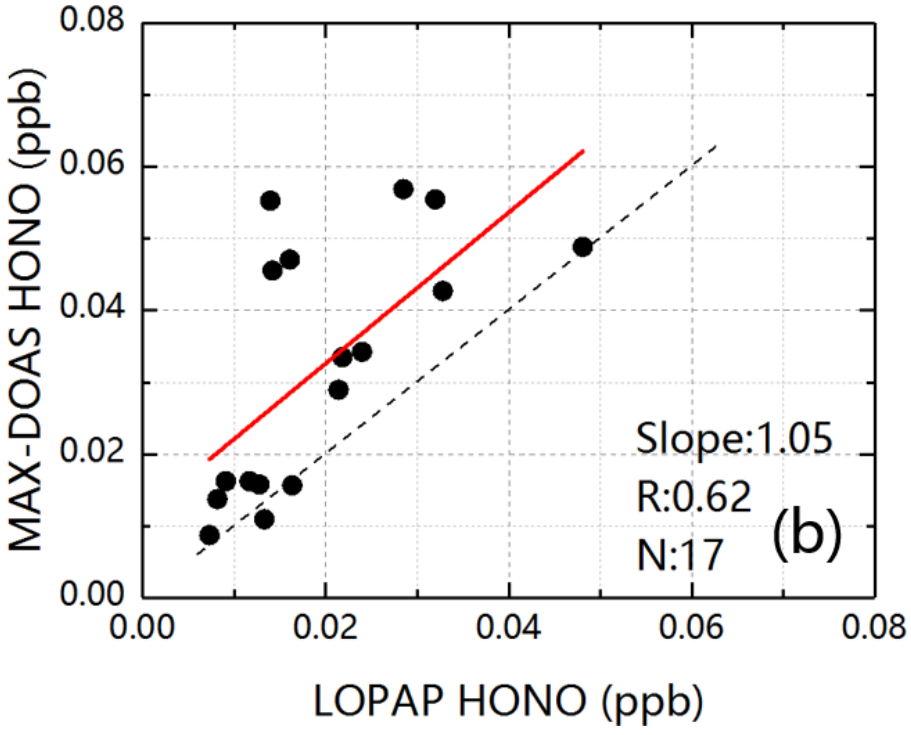

Figure R1-5 Validtons of the MAX-DOAS HONO vs. LOPAP HONO (Xing et al., 2024c)

4) The heterogeneous formation of HONO from NO_2 uptake on wet (aerosol) surfaces can be a source of HONO. However, this HONO will only degas under certain conditions (enhanced acidity, drying / evaporation of water from the aerosol up to crystallisation thresholds). Otherwise, the HONO will not be a gas phase reservoir and consequently a potential gaseous OH source. If aerosol HONO will photolyse also the produced OH will react in the aerosol phase and not degas to contribute to "classical" (= gas phase) oxidation capacity.

Re: Thank you for your comments.

(1) Due to the inherent limitations of the DOAS technique, our measurements are restricted to the gaseous phase of HONO. This represents a well-recognized limitation within the broader DOAS research community.

(2) Within the field of DOAS research, it is standard practice to employ a consistent methodological framework to assess the capacity of HONO to generate OH. For instance, Alicke et al., (2002) utilized synchronous DOAS measurements of HONO/NO_2 and J(HONO) to quantify that HONO photolysis can exceed O_3 photolysis as an OH source during morning hours, accounting for approximately 20% of the total OH production over the course of a day. Furthermore, Rohrer et al., (2005) integrated DOAS retrievals with surface observations to demonstrate the existence of an unknown daytime heterogeneous or photo-enhanced HONO source, thereby establishing HONO photolysis as a critical driver of atmospheric oxidation capacity throughout the entire diurnal cycle, rather than being confined to the morning period.

(3) Your concerns (HONO being retained within particles for photolysis and OH being restricted to the particle-phase oxidation) are partially valid under extremely high humidity/haze conditions, but the evidence chain of this study (the Yangtze-Huai River Basin in spring and summer, the mid-boundary layer of the city) supports the dominance of gas-phase release, as argued below:

① Heterogeneous formation and degassing kinetics: The fate of HONO after generation on aerosols or surfaces depends on the Henry's law constant, pH, RH, and particle size. The mid-level of the urban boundary layer (2.4 km, summer) has a typical RH of 60–75% and is in a non-saturated hygroscopic state; aerosols are mostly externally mixed, containing black carbon/mineral dust interfaces that promote HONO desorption. Villena et al. (2011) pointed out that even in cold and dry environments, surface HONO formation can still achieve a net release of OH precursors. More critically, Cheng et al., (2025) demonstrated through high-tower vertical measurements that daytime upper-level (>300 m) HONO is positively correlated with NO_2 and aerosol extinction, is independent of surface emissions, and the HONO/NO_2 ratio peaks with altitude, corroborating heterogeneous conversion and gas-phase release. If HONO were trapped

within particles, it would be impossible to explain this vertical gradient.

② Closed-loop observational evidence: This study found a HONO enhancement layer at 2.4 km in the summer city (Figures 3 and 4 in the manuscript), with C(HONO) = 0.053 h^{-1}, corresponding to a weight of up to 30.6% (Figure 7). If HONO were not released, MAX-DOAS could not detect this gas-phase HONO layer (DOAS measures atmospheric column gas-phase absorption; dense fog is an exception but requires Mie scattering correction, which we have already addressed using O_4-retrieved aerosols input into VLIDORT). Xing et al., (2023) specifically compared inland and coastal areas, finding that the mid-level HONO enhancement in inland cities coincides with the aerosol layer, and the photolysis of particle-phase HONO cannot explain the gas-phase OH production rate gap; it must be released into the gas phase. Furthermore, Zhang et al., (2023) found in a winter haze study that the HONO production on aerosol surfaces is massive, and the daytime HONO budget gap can only be filled by particle-phase release.

③ Indirect contribution of particle-phase OH: Even if some HONO photolyzes within particles to produce OH, the oxidation of VOCs/SO_2 by particle-phase OH also generates low-volatility products (SOA/SIA), which still requires gas-phase OH to initiate the VOC oxidation chain. Moreover, AOC is strongly correlated with aerosols (R = 0.88–0.93, Figure 8): regardless of which phase OH is generated in, it ultimately drives the transformation of gas-phase precursors to particles. Our calculation is based on the gas-phase HONO concentration (measured by MAX-DOAS); if HONO were within the particles, it would not contribute to this signal. Therefore, the OH peak in the figure directly proves the existence of gas-phase HONO. In summary, attributing the mid-level HONO to heterogeneous conversion followed by release for gas-phase photolysis to produce OH is the most parsimonious self-consistent explanation constrained by observations.

5) The boundary layer height is not discussed at all throughout the manuscript. Even though the trace gas profiles show distinct characteristics of the diurnal boundary layer, especially in summer for HCHO, this effect is not considered or discussed at all, e.g., whether the O_3 related OH production is only happening above the PBL and whether the vertical gradients in the considered compounds are related to the PBL dynamics. A distinction between a morning boundary layer and potential effects of the residual layer from the previous day(s) is not done, even though Fig 2. indicates this, e.g., double peaks for HCHO at AHU and complex structure of O_3 in the lowest 1.5 kilometers, which can originate from the chemical effects as well as from boundary layer dynamics.

***Re*:** Thank you for your comments.

(1) We have added PBLH data and related analyses. Our failure to adequately discuss this important factor in the initial draft was indeed an oversight. The PBLH is shown in Figure R1-6. The PBLH data were derived from the ERA5 reanalysis dataset, and the diurnal variation of the PBLH is illustrated in Figure R1-6. Additional PBLH data have been provided in Figure S7 of the Supplementary Material.

(2) The detailed supplements and revisions are as follows:

① Diurnal variation and seasonal characteristics of PBLH: Spring (a1, b1): PBLH begins to rise from about 0.3–0.4 km at 08:00, reaching a peak (about 1.2–1.3 km) in the afternoon at 14:00–15:00, followed by a gradual decline. The lower PBLH and slower development in spring reflect the characteristics of weaker solar radiation and convective activity. Summer (a2, b2): PBLH exhibits a larger rising magnitude, with peak heights reaching 1.0–1.2 km and maintaining for a longer duration (around 12:00–16:00). The higher PBLH and more vigorous development in summer are entirely consistent with the intense convective activity driven by strong solar radiation and surface heating.

② Physical control of PBLH on the vertical distribution of pollutants: The thermodynamics of the boundary layer directly shape the vertical structures of HCHO, O_3, and HONO through two mechanisms: “mixing dilution” and “uplift transport”. “Near-surface accumulation effect” of low spring PBLH: The lower PBLH in spring (<1.3 km) causes pollutants to hardly diffuse upward. At the AHU urban site, high near-surface NOx concentrations (traffic emissions) strongly suppress O_3 through NO titration (Figure 2c1), forming a “low-level O_3 trough”; whereas HONO forms a “near-surface high-value layer” (Figure 2a1) due to surface emissions and heterogeneous conversion. At the CF rural site, the weaker PBLH development in spring causes HCHO from biogenic emissions to be mainly concentrated near the surface (Figure 2b1), forming a typical biogenic characteristic of “near-surface high values–rapid high-altitude attenuation”. “Vertical homogenization effect” of high summer PBLH: The significantly raised PBLH in summer (>1 km) and vigorous convective mixing transport surface-emitted VOCs (e.g., HCHO) and secondarily generated pollutants upward throughout the boundary layer (Figure 2b5). At the AHU urban site, HCHO transitions from the spring pattern of “near-surface high values–rapid high-altitude attenuation” to a “vertically homogenized distribution” in summer (Figure 2b5), which serves as physical evidence of boundary layer mixing. Meanwhile, the summer PBLH uplift causes the residual layer to be entrained, and O_3 and HCHO accumulated in the residual layer from the previous day are mixed downward, forming a “mid-level O_3 high-value zone” (Figure 2c5).

③ Vertical coupling of O_3-related OH production and PBLH. O_3 photolysis-dominated OH

production and PBLH dynamics exhibit a significant vertical coupling relationship: Near-surface "NO titration suppression zone": At the bottom of the PBL (<1 km), in both spring and summer, high NOx concentrations suppress O_3 through NO titration, resulting in an extremely low OH production contribution from O_3 photolysis (Figure 6c1, 6c2). This phenomenon is directly related to the "near-surface mixing dilution" mechanism of PBLH—fresh NOx emissions are confined to the lower layer, forming a chemical suppression zone. Mid-PBL "O_3 accumulation zone": In the mid-PBL (1–2 km), as altitude increases, NOx rapidly attenuates due to chemical reactions and diffusion, while O_3 gradually accumulates due to photochemical production and vertical transport (Figure 2c5). At this point, the OH production contribution from O_3 photolysis increases significantly (Figure 6c2), which perfectly matches the physical process of "mid-level mixing transport" after PBLH uplift. PBL top "residual layer chemistry zone": At the PBL top (>2 km), the summer PBLH uplift causes the residual layer to be entrained, and O_3 and HONO accumulated in the residual layer become important sources for OH production (Figure 6a2, 6c2). This "vertical chemical stratification" phenomenon (lower-layer HONO/HCHO dominance vs. upper-layer O_3 dominance) is precisely the result of the coupling between PBLH dynamics and photochemical processes.

④ Chemical distinction between the boundary layer and the residual layer: The "distinction between the morning boundary layer and the residual layer" you mentioned in the question is clearly reflected in our data: Morning "residual layer residue": In the early stage of PBL development (08:00–10:00), the boundary layer height is low, and pollutants (e.g., O_3, HCHO) in the residual layer from the previous day have not yet been completely mixed. At the AHU urban site, a "sub-peak" of spring morning O_3 appears at an altitude of 0.5–1 km (Figure 2c1), which is exactly the residual signal of residual layer chemistry. Afternoon "full-layer mixing": As PBLH reaches its peak in the afternoon (14:00–15:00), pollutants within the boundary layer are fully mixed, and vertical gradients tend to flatten (Figure 2b5, 2c5). At this time, chemical processes (e.g., HCHO photolysis, O_3 production) dominate the pollutant distribution, while the influence of physical mixing weakens.

⑤ Revisions and deepening of the original conclusions: Combining the PBLH data, we have made the following revisions and deepening to the original conclusions:

a) Section 3.1 (Overview) of the original text: When discussing the vertical structure, it is explicitly stated that "the spring boundary layer is controlled by local emissions and near-surface chemical titration; the summer boundary layer is affected by vigorous convective mixing and residual layer chemistry". PBLH data are supplemented as physical evidence,

illustrating that the vertical distribution of pollutants is the result of the joint action of "chemical processes + physical mixing".

b) Section 3.4 (OH produced from HONO, HCHO and O_3) of the original text: In explaining the vertical stratification of OH production, it is explicitly stated that "the lower-layer HONO/HCHO dominance is the result of near-surface emissions and NO titration; the upper-layer O_3 dominance is the result of NOx attenuation and O_3 accumulation after PBLH uplift".

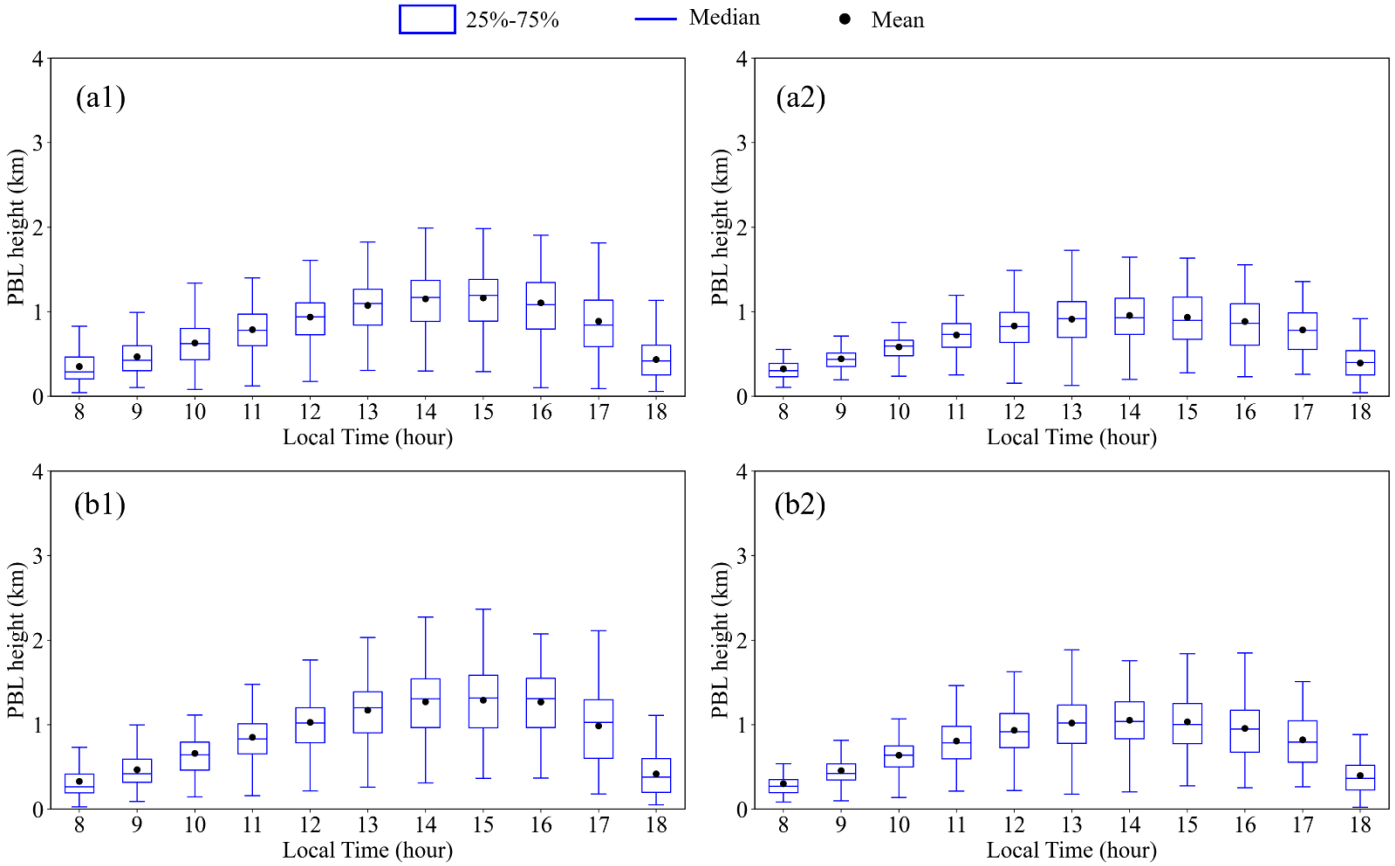

Figure R1-6. PBLH at (a1) AHU site in spring; (a2) AHU site in summer; (b1) CF site in spring; (b2) CF site in summer.

6) How is cloudiness taken into account in the measurements? DOAS retrievals will only be possible to a certain degree under cloudy or broken-cloudy conditions, substantially influencing the retrieval. Does this cause a sampling bias, e.g., in the afternoon hours with more active continental convective activity?

***Re*:** Thank you for your comments. Clouds (particularly low broken clouds) alter the multiple scattering of the optical path and must be strictly filtered out. Our preprocessing includes multi-tier cloud and quality screening. Section 2.2 of the original manuscript briefly mentioned SZA < 75° and RMS filtering; the revised version will provide a detailed process, described as follows:

(1) Cloud detection based on O_4 and Color Index (CI): O_4 DSCD outliers: Clouds cause a dramatic increase in the optical path length, leading to a sudden jump in O_4 DSCDs (which are positively correlated with

aerosol loading / optical path). We rejected data points within a single scan where the O_4 DSCD > mean + 2σ or the coefficient of variation > 30% (Gielen et al., 2013; Xing et al., 2017). Color Index, Clouds or thick aerosols cause a decrease in CI and a convergence across different elevation angles. Thresholds were set as follows: a CI variation > 5% or CI < 0.5 (typically > 0.8 for clear skies) was identified as cloud contamination (Wagner et al., 2013).

(2) Dual filtering by RMS and DOF: The spectral fitting RMS ≤ 1×10^{-3} (Section 2.2 of the manuscript) has already excluded the majority of optical distortions (clouds induce large fitting residuals). Scans with DOF < 1.0 were rejected (insufficient information content, likely due to cloud contamination or aerosol abrupt changes violating the horizontal homogeneity assumption) (Hendrick et al., 2014).

(3) Bias assessment of afternoon convective clouds: In Hefei during spring and summer afternoons (13–15 LT), cumulus clouds develop, resulting in a data retention rate of ~60–70% (consistent with the Shanghai observations by Xing et al., 2017). This constitutes random missing data (retrieval failure/rejection when clouds are present), rather than a systematic high bias (O_3 under clouds might be high but cannot be measured due to chaotic light scattering; clear-sky data are retained).

(4) Literature support: Wagner et al., (2013) demonstrated that the MAX-DOAS inherent CI and O_4 can efficiently identify clouds; in CINDI-2 (Wang et al., 2020), all participants adopted similar cloud screening, ensuring reliable data quality. We will add relevant statements to the manuscript.

7) What is the data source for the NO, NOx or NO_2 data? What are the corresponding uncertainty limits? Is NO_2 also retrieved from the DOAS? Or is it just a surface measurement, only available at one location? How is the secondary HONO determined at the other location if there is no NOx data? And how are the C_HONO t values containing the HONO to NO_X ratios in Fig.4 calculated? If NOx is determined from an assumed constant(?) ratio of HONO/NOx, then this has a very high uncertainty. On the other hand, using this relation afterwards to determine C_HONO would not allow for any variability in NOx independent of HONO.

***Re*:** Thank you for your comments.

(1) Data source for NO, NO_X, or NO_2: The NO_2 data utilized in this study were retrieved from our instrumental measurements, and the corresponding vertical profiles are illustrated in Figure R1-7 (Figure S8 in the supplemental material). Considering that our instrument is incapable of directly measuring NO, the NO concentrations were derived via a chemical conversion relationship. The detailed conversion procedure is described in Section S2 (“Direct emission of HONO”) of the supplemental material, with the specific contents as follows: In this study, NOx could not be measured directly. To obtain NOx data, we applied methods reported in previous studies (Mannschreck et al., 2004; Shetter et al., 1983), as described below. During daytime, under sunlight, NO, NO_2, and O_3 rapidly reach quasi-steady state (photostationary state) through the following fast reversible reactions:

$$NO + O_3 \xrightarrow{k} NO_2 + O_2 \quad \text{(S6)}$$

$$NO_2 + h\nu \xrightarrow{J_{NO2}} NO + O(^3P) \quad \text{(S7)}$$

Under typical urban atmospheric conditions (within a few minutes), this cycle can be approximately considered at steady state, and the concentrations of NO, NO_2, and O_3 satisfy the following relationship:

$$[NO] = \frac{J_{NO2}}{k} \times \frac{[NO_2]}{[O_3]} \quad \text{(S8)}$$

where [NO], [NO_2], and [O_3] represent the concentrations of NO, NO_2, and O_3, respectively; J_{NO2} is the photolysis frequency of NO_2; and k is the reaction rate constant of NO with O_3 (Eq. S6), calculated using the Arrhenius equation (Eq. S9) as a temperature-dependent value:

$$k(T) = A \cdot e^{-Ea/(RT)} \quad \text{(S9)}$$

Daytime NO concentrations were estimated from the NO–NO_2–O_3 photostationary-state relationship. To minimise uncertainty, only data collected between 11:00 and 15:00 were used.

(2) Uncertainty: The uncertainty associated with NO_2 originates from the DOAS retrieval process. Calculated using the identical methodology as described in our response to Comment 3), the total uncertainty for NO_2 is determined to be 26%. Within the DOAS community, this level of uncertainty is entirely acceptable and well-documented in the literature (Hendrick et al., 2014; Kreher et al., 2020; Xing et al., 2023). In our future studies, we aim to further enhance the retrieval precision of the instrument to continually reduce this uncertainty.

(3) The NO_2 presented here comprises vertical profile data (Figure R1-7). The retrieval methodology is identical to that employed for other trace gases such as HONO, O_3, and HCHO. As this method has been comprehensively detailed in our response to Comment 1), we omit further elaboration here.

(4) We have explicitly excluded the influence of direct HONO emissions at the AHU site. Conversely, at the CF site, such exclusion was not performed due to the lack of available NO_X data. The primary justification for this is that at the rural agricultural CF site, direct NO_X emissions from vehicular traffic are negligibly low, while soil-emitted HONO (Xue et al., 2021, 2022) is likely the dominant source. Therefore, in the calculation of $C_{(HONO)}$ at the CF site, the values primarily reflect the conversion potential of NO_2 to HONO and the apparent conversion rate that may be influenced by soil emissions.

(5) Calculation of $C_{(HONO)}$: This parameter was calculated using the following equation (Wentzell et al., 2010; Xing et al., 2024b), where [HONO] and [NO_2] denote the respective concentrations of HONO and NO_2. Both variables are derived from the instrumental retrievals and are strictly paired to match identical timestamps and altitudes during the computation.

$$C_{(HONO)} = \frac{\frac{[HONO]_{t_2}}{[NO_2]_{t_2}} - \frac{[HONO]_{t_1}}{[NO_2]_{t_1}}}{t_2 - t_1} \quad \text{(S10)}$$

The time interval ($t_2 - t_1$) in the equation does not have an absolute, fixed standard; rather, it depends on the specific objectives of the study (e.g., nocturnal averaging or a specific growth period) and the temporal resolution of the dataset. In analogous studies within the field, the most prevalent approach is to adopt a 1-hour time interval (Alicke et al., 2002; Wentzell et al., 2010; Xing et al., 2024b), which is the interval adopted in the present study.

(6) It should be emphasized that NO_X does not represent a constant value; rather, it is dynamically derived as addressed in our response to point (1). Our instrument provides the NO_2 measurement, from which NO is subsequently calculated via the conversion relationship. NO_X is then determined as the sum of NO_2 and NO. Consequently, NO_X is not a constant but a variable quantity that tracks the vertical variability of the NO_2 profile. We acknowledge that the current study possesses certain inherent limitations, yet this approach is a widely adopted convention in comparable research. In subsequent studies, we plan to deploy dedicated NO_X instrumentation to further refine the research accuracy.

We will explicitly clarify these points in the revised manuscript to preclude any potential misunderstanding.

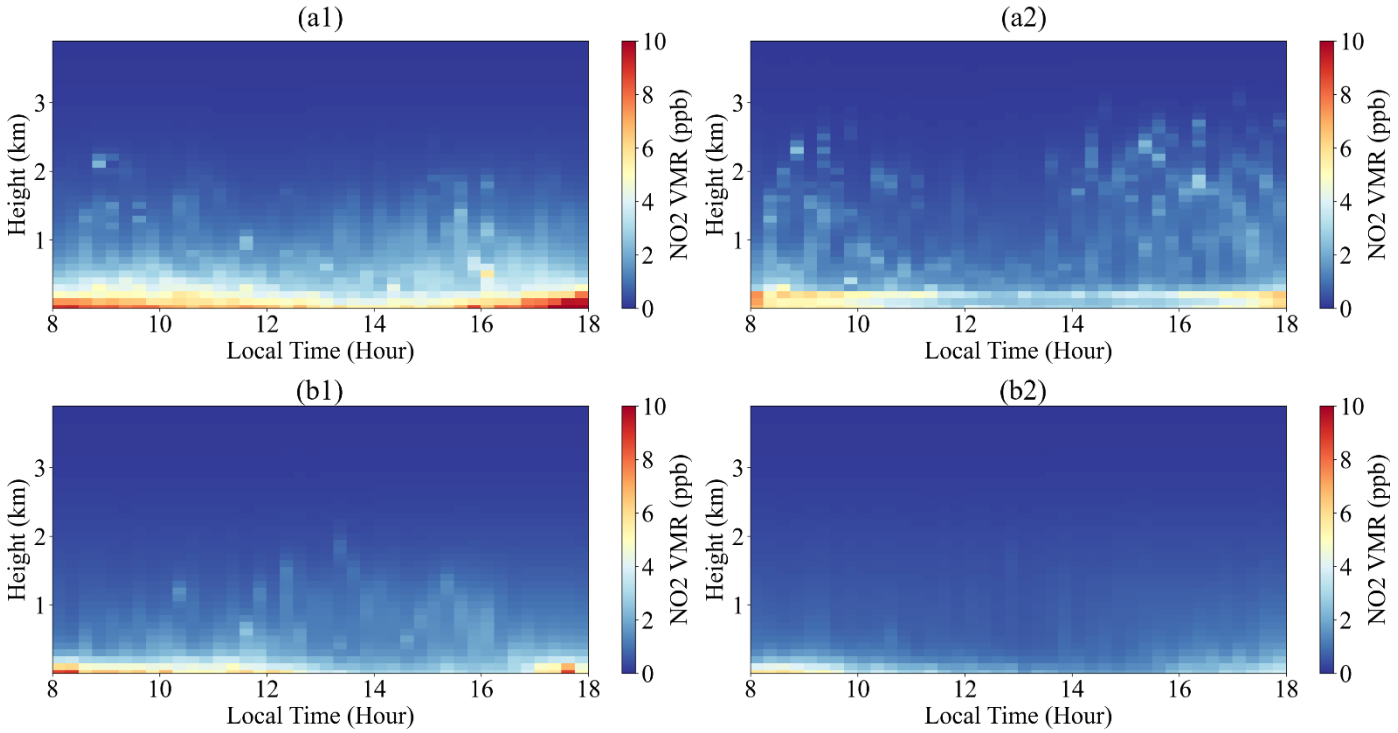

Figure R1-7. Seasonal mean vertical profiles of NO_2. (a1) AHU site in spring; (a2) AHU site in summer; (b1) CF site in spring; (b2) CF site in summer.

8) The Chapter about daytime O_3 sources should in my opinion be removed, as it does not really contribute to the question of OH abundance and the sources of OH. If it is supposed to remain in the manuscript it must be substantially modified as at the moment the conclusions are in my opinion erroneously formulated. The

analysis shows that near the surface there is a lot of NOx and HONO (being a primary OH source), therefore the conclusion that this region is NOx limited is simply wrong (Fig.5). If there is more NOx than HCHO in the determination of the FNR, then the system is VOC limited and not NOx limited. At maximum, the lowermost layers with enhanced HONO (and consequently NOx) are transition of even VOC limited. In the layers above the surface in summer, the authors state that this is a NOx limited regime, but do not provide any information where the NOx data have been derived from! In spring, the analysis states that in the lower layers, there is a VOC limitation which is not that obvious from Fig. 2m which shows also in spring and most dominant substantial HCHO mixing ratios in altitudes up to 1.5 km altitude. All of this appears in either a transition regime. If this kind of analysis is conducted you have to have proper NOx vertical profiles and show the FNR instead! If the results are intended to show different things than those which I interpreted from the graphic, then this should be substantially clarified.

***Re*:** Thank you for your comments.

(1) We have removed this section from the revised manuscript.

(2) In response to your concern regarding this issue, we provide the following clarification.

① Clarification of definitions and NO_2 data source: The reviewer pointed out that "high near-surface HONO/NOx should be VOC-limited, making the conclusion of NOx-limited contradictory." We need to reiterate the classic definition of the FNR ($HCHO/NO_2$) threshold method: a high FNR (large $HCHO/O_3$) indicates relatively scarce NOx and NOx-limited conditions; a low FNR indicates VOC-limited conditions. Our thresholds in Figure 5 (AHU: 1.48–1.88, CF: 1.04–1.76) are based on the normalized slope method (Li et al., 2024; Lin et al., 2022), not arbitrary fixed values. The key point: NO_2 is not a single surface point! As detailed in our Response 7, NO_2 has a vertical profile (retrieved from the same source), and the FNR in Figure 5 is the ratio of HCHO to NO_2 at corresponding altitudes for each layer, not an extrapolation of surface NO_2. Summer AHU 0–2 km: high near-surface NO_2 (urban emissions, weak titration consuming O_3), low FNR (<1.48), NOx-limited (consistent with the definition: adding NOx suppresses O_3 due to strong NO titration); 2–4 km NO_2 exponentially decays to <5 ppb, HCHO is maintained at ~1 ppb due to VOC oxidation, FNR >1.88, VOC-limited. Spring overall FNR ~1.5 (transition). This vertical reversal has been reported in Lin et al., (2022) and Li et al., (2024) (NOx-limited at lower layers, VOC-limited at upper layers). The failure of the initial draft to explicitly state "NO_2 profiles from MAX-DOAS" was a major omission; the revision will clarify this and append the NO_2 profile figure. CF 0–1 km NO_2 is lower (few sources in rural areas) but HCHO is high (biogenic VOCs), FNR is occasionally high but strongly influenced by NO_2 fluctuations (threshold 1.04–1.76), hence 0–1 km NOx-limited (low FNR), 1–2.5 km transitional, >2.5 km VOC-limited. Figure 2 (CF

HCHO in spring) shows high HCHO at 0–1.5 km, but if NO_2 is synchronously high (near the surface), the FNR is not necessarily high, belonging to a transitional/NOx-limited regime, rather than purely VOC-limited.

② Section 3.3 is not redundant; it explains why the OH pathway exhibits vertical differentiation. The lower-layer NOx-limited regime implies that HONO/HCHO compete for OH and NO titration suppresses O_3 photolysis; the upper-layer VOC-limited regime implies that O_3 photolysis proceeds unhindered, becoming the primary OH source. This supports the pattern in Section 3.4 of "<1 km HONO/HCHO dominance, >2.8 km O_3 dominance." If deleted, the vertical transition of OH would lose the context of precursor sensitivity.

9) The link to the aerosol particles in 3.5 are over-simplifying the aerosol system in my point of view. If all the aerosol would originate from oxidised organics, this relation could hold. However, no chemical analysis of the aerosol is undertaken. Consequently, especially the urban aerosol will contain many additional compounds (sulfate, nitrate, ammonium) which is only indirectly affected by the oxidation capacity and therefore those connections are only weak and can be dominated by the effects of e.g., boundary layer height and boundary layer mixing. The correlation between AOC and aerosols can therefore originate from co-correlated variables and not necessarily from the chemical relations.

***Re*:** Thank you for your comments.

(1) This represents a limitation of our current study, which fundamentally stems from the inherent constraints of the DOAS technique itself. In our future work, we aim to address this issue through the development of Polarization DOAS. The incorporation of polarimetric capabilities is expected to effectively resolve the issue you raised, as it holds the potential to discriminate various aerosol components. The development of this Polarization DOAS system is currently underway.

(2) High correlation coefficients alone cannot prove unidirectional chemical causality; boundary layer height, convective mixing, and meteorological conditions can indeed simultaneously modulate AOC and aerosol extinction. In the revised manuscript, we will revise the original sentence "AOC promotes secondary aerosol formation" to: "AOC and aerosol loading exhibit strong vertical covariation (R=0.88–0.93), a relationship that is jointly modulated by boundary layer dynamics and is also consistent with the coherent physical chain of oxidative capacity driving the conversion of gaseous precursors (VOCs, SO_2, NO_X) to secondary particles." The following points use published literature to demonstrate the rationality of this statement.

① The AOC–secondary aerosol coupling is a classic conclusion in atmospheric chemistry, not an original simplification of this paper. Numerous observation- and model-based studies have

confirmed that enhanced AOC significantly increases the fractions of SOA and nitrate/sulfate in $PM_{2.5}$. Feng et al., (2020) (WRF-Chem simulation in the Guanzhong Basin) reported $\Delta PM2.5/\Delta AOC \approx 1.94\ \mu g \cdot m^{-3}$ / ($10^6\ cm^{-3}s^{-1}$), with SOA accounting for 43% and nitrate for 40%. Zhou et al., (2024) pointed out that low AOC (MDA8 $O_3 \leq 100\ \mu g \cdot m^{-3}$) promotes the oxidation of VOCs to form secondary particles, and Ox is significantly correlated with SOR/NOR. Dai et al., (2023) explicitly defined AOC as the total reaction rate of oxidants, with >90% of daytime AOC coming from the reactions of OH with VOCs/CO, directly linking it to the formation of SOA and SNA. These studies mostly used surface or column totals; this paper uses MAX-DOAS to advance this chain to the vertical dimension.

② Covariation with PBL dynamics ≠ negation of the chemical chain. We acknowledge that the contraction/expansion of PBLH simultaneously alters J values, mixing, and extinction. However, multiple vertically resolved MAX-DOAS studies have demonstrated that the aerosol–OH precursor relationship contains process-level chemical components: He et al., (2023) (Shanghai suburbs) found that the HONO high-value layer at ~0.7 km is positively correlated with aerosol extinction, attributing this to photo-enhanced heterogeneous conversion on aerosol surfaces. Xing et al., (2024b) showed that HONO/NO_2 peaks occur in layers with aerosol extinction >0.15 km^{-1} (<1 km) or >0.02 km^{-1} (1–2 km), directly linking heterogeneous conversion to the vertical aerosol structure. Cheng et al. (Guangzhou 450 m tower) (Cheng et al., 2025) demonstrated that the contribution of in situ NO+OH production to the HONO budget within the urban boundary layer increases with altitude, while the weight of surface processes decreases. This indicates that the "aerosol–OH/HONO" relationship cannot be explained by PBLH alone.

③ The vertical structure of Figure 7 in this paper itself supports the chemical explanation: The correlation between AOC and aerosols varies with altitude: R≈0.93 near the surface (0–0.5 km), decreasing to ≈0.88 at 2–3 km. If purely dominated by PBL dilution, the correlation across layers should be uniform; the stronger coupling near the surface exactly corresponds to the highly reactive zones of near-source emissions, HONO/HCHO photolysis, and SOA/SNA, consistent with the compositional conclusions of Feng et al., (2020) and Zhou et al., (2024). The rural CF site, where biogenic HCHO drives OH ($P(OH)HCHO=1.82\times10^{-3}\ ppb \cdot s^{-1}$), also supports the biogenic SOA chain.

References

Alicke, B., Platt, U., and Stutz, J.: Impact of nitrous acid photolysis on the total hydroxyl radical budget during the Limitation of Oxidant Production/Pianura Padana Produzione di Ozono study in Milan, Journal of Geophysical Research: Atmospheres, 107, LOP 9-1-LOP 9-17, https://doi.org/10.1029/2000JD000075, 2002.

Cheng, P., Ling, J., Gong, Y., Yang, W., Wang, S., Han, B., Li, X., Yuan, B., Pei, C., Shen, J., Yu, Y., Huang, L., Deng, H., and Liu, Z.: Understanding Nitrous Acid (HONO) in the Urban Boundary Layer Using Continuous HONO Measurements at a 450 m Tall Tower in Guangzhou, China, Environ. Sci. Technol., 59, 10411–10421, https://doi.org/10.1021/acs.est.4c14279, 2025.

Dai, J., Brasseur, G. P., Vrekoussis, M., Kanakidou, M., Qu, K., Zhang, Y., Zhang, H., and Wang, T.: The atmospheric oxidizing capacity in China – Part 1: Roles of different photochemical processes, Atmospheric Chemistry and Physics, 23, 14127–14158, https://doi.org/10.5194/acp-23-14127-2023, 2023.

Feng, T., Zhao, S., Zhang, X., Wang, Q., Liu, L., Li, G., and Tie, X.: Increasing wintertime ozone levels and secondary aerosol formation in the Guanzhong basin, central China, Science of The Total Environment, 745, 140961, https://doi.org/10.1016/j.scitotenv.2020.140961, 2020.

Friedrich, M. M., Rivera, C., Stremme, W., Ojeda, Z., Arellano, J., Bezanilla, A., García-Reynoso, J. A., and Grutter, M.: NO_2 vertical profiles and column densities from MAX-DOAS measurements in Mexico City, Atmospheric Measurement Techniques, 12, 2545–2565, https://doi.org/10.5194/amt-12-2545-2019, 2019.

Frieß, U., Monks, P. S., Remedios, J. J., Rozanov, A., Sinreich, R., Wagner, T., and Platt, U.: MAX-DOAS O4 measurements: A new technique to derive information on atmospheric aerosols: 2. Modeling studies, Journal of Geophysical Research: Atmospheres, 111, https://doi.org/10.1029/2005JD006618, 2006a.

Frieß, U., Monks, P. S., Remedios, J. J., Rozanov, A., Sinreich, R., Wagner, T., and Platt, U.: MAX-DOAS O4 measurements: A new technique to derive information on atmospheric aerosols: 2. Modeling studies, Journal of Geophysical Research: Atmospheres, 111, https://doi.org/10.1029/2005JD006618, 2006b.

Frieß, U., Beirle, S., Alvarado Bonilla, L., Bösch, T., Friedrich, M. M., Hendrick, F., Piters, A., Richter, A., van Roozendael, M., Rozanov, V. V., Spinei, E., Tirpitz, J.-L., Vlemmix, T., Wagner, T., and Wang, Y.: Intercomparison of MAX-DOAS vertical profile retrieval algorithms: studies using synthetic data, Atmospheric Measurement Techniques, 12, 2155–2181, https://doi.org/10.5194/amt-12-2155-2019, 2019.

Fu, D., Song, Z., Zhang, X., Wu, Y., Duan, M., Pu, W., Ma, Z., Quan, W., Zhou, H., Che, H., and Xia, X.: Similarities and Differences in the Temporal Variability of PM2.5 and AOD Between Urban and Rural Stations in Beijing, Remote Sensing, 12, https://doi.org/10.3390/rs12071193, 2020.

Gielen, C., Van Roozendael, M., Hendrick, F., Fayt, C., Hermans, C., Pinardi, G., and Vlemmix, T.: Development of a cloud-screening method for MAX-DOAS measurements, 7153, 2013.

Guo, J., Xia, F., Zhang, Y., Liu, H., Li, J., Lou, M., He, J., Yan, Y., Wang, F., Min, M., and Zhai, P.: Impact of diurnal variability and meteorological factors on the PM2.5 - AOD relationship: Implications for PM2.5 remote sensing, Environmental Pollution, 221, 94–104, https://doi.org/10.1016/j.envpol.2016.11.043, 2017.

He, S., Wang, S., Zhang, S., Zhu, J., Sun, Z., Xue, R., and Zhou, B.: Vertical distributions of atmospheric HONO and the corresponding OH radical production by photolysis at the suburb area of Shanghai, China, Science of The Total Environment, 858, 159703, https://doi.org/10.1016/j.scitotenv.2022.159703, 2023.

Hendrick, F., Müller, J.-F., Clémer, K., Wang, P., De Mazière, M., Fayt, C., Gielen, C., Hermans, C., Ma, J. Z., Pinardi, G., Stavrakou, T., Vlemmix, T., and Van Roozendael, M.: Four years of ground-based MAX-DOAS observations of HONO and NO_2 in the Beijing area, Atmospheric Chemistry and Physics, 14, 765–781, https://doi.org/10.5194/acp-14-765-2014, 2014.

Jiao, P., Xing, C., Li, Y., Ji, X., Tan, W., Li, Q., Liu, H., and Liu, C.: A dataset of ground-based vertical profile observations of aerosol, NO_2, and HCHO from the hyperspectral vertical remote sensing network in China (2019–2023), Earth System Science Data, 17, 3167–3187, https://doi.org/10.5194/essd-17-3167-2025, 2025.

Kramer, L. J., Crilley, L. R., Adams, T. J., Ball, S. M., Pope, F. D., and Bloss, W. J.: Nitrous acid (HONO) emissions under real-world driving conditions from vehicles in a UK road tunnel, Atmospheric Chemistry and Physics, 20, 5231–5248, https://doi.org/10.5194/acp-20-5231-2020, 2020.

Kreher, K., Van Roozendael, M., Hendrick, F., Apituley, A., Dimitropoulou, E., Frieß, U., Richter, A., Wagner, T., Lampel, J., Abuhassan, N., Ang, L., Anguas, M., Bais, A., Benavent, N., Bösch, T., Bognar, K., Borovski, A., Bruchkouski, I., Cede, A., Chan, K. L., Donner, S., Drosoglou, T., Fayt, C., Finkenzeller, H., Garcia-Nieto, D., Gielen, C., Gómez-Martín, L., Hao, N., Henzing, B., Herman, J. R., Hermans, C., Hoque, S., Irie, H., Jin, J., Johnston, P., Khayyam Butt, J., Khokhar, F., Koenig, T. K., Kuhn, J., Kumar, V., Liu, C., Ma, J., Merlaud, A., Mishra, A. K., Müller, M., Navarro-Comas, M., Ostendorf, M., Pazmino, A., Peters, E., Pinardi, G., Pinharanda, M., Piters, A., Platt, U., Postylyakov, O., Prados-Roman, C., Puentedura, O., Querel, R., Saiz-Lopez, A., Schönhardt, A., Schreier, S. F., Seyler, A., Sinha, V., Spinei, E., Strong, K., Tack, F., Tian, X., Tiefengraber, M., Tirpitz, J.-L., van Gent, J., Volkamer, R., Vrekoussis, M., Wang, S., Wang, Z., Wenig, M., Wittrock, F., Xie, P. H., Xu, J., Yela, M., Zhang, C., and Zhao, X.: Intercomparison of NO_2, O_4, O_3 and HCHO slant column measurements by MAX-DOAS and zenith-sky UV–visible spectrometers during CINDI-2, Atmospheric Measurement Techniques, 13, 2169–2208, https://doi.org/10.5194/amt-13-2169-2020, 2020.

Li, S., Song, W., Zhan, H., Zhang, Y., Zhang, X., Li, W., Tong, S., Pei, C., Wang, Y., Chen, Y., Huang, Z., Zhang, R., Zhu, M., Fang, H., Wu, Z., Wang, J., Luo, S., Fu, X., Xiao, S., Huang, X., Zeng, J., Zhang, H., Chen, D., Gligorovski, S., Ge, M., George, C., and Wang, X.: Contribution of Vehicle Emission and NO2 Surface Conversion to Nitrous Acid (HONO) in Urban Environments: Implications from Tests in a Tunnel, Environ. Sci. Technol., 55, 15616–15624, https://doi.org/10.1021/acs.est.1c00405, 2021.

Li, Y., Xing, C., Hong, Q., Jiao, P., Peng, H., Tang, Z., and Liu, C.: Ozone Formation Sensitivity at Various Altitudes: Seeking the Optimal Method for Sensitivity Threshold Determination, Environ. Sci. Technol. Lett., 11, 1334–1339, https://doi.org/10.1021/acs.estlett.4c00777, 2024.

Liao, Z., Gao, M., Zhang, J., Sun, J., Quan, J., Jia, X., Pan, Y., and Fan, S.: Mixing-layer-height-referenced ozone vertical distribution in the lower troposphere of Chinese megacities: stratification, classification, and meteorological and photochemical mechanisms, Atmospheric Chemistry and Physics, 24, 3541–3557, https://doi.org/10.5194/acp-24-3541-2024, 2024.

Lin, H., Xing, C., Hong, Q., Liu, C., Ji, X., Liu, T., Lin, J., Lu, C., Tan, W., Li, Q., and Liu, H.: Diagnosis of Ozone Formation Sensitivities in Different Height Layers via MAX-DOAS Observations in Guangzhou, Journal of Geophysical Research: Atmospheres, 127, e2022JD036803,

https://doi.org/10.1029/2022JD036803, 2022.

Mannschreck, K., Gilge, S., Plass-Duelmer, C., Fricke, W., and Berresheim, H.: Assessment of the applicability of NO-NO_2-O_3 photostationary state to long-term measurements at the Hohenpeissenberg GAW Station, Germany, Atmospheric Chemistry and Physics, 4, 1265–1277, https://doi.org/10.5194/acp-4-1265-2004, 2004.

Orphal, J. and Chance, K.: Ultraviolet and visible absorption cross-sections for HITRAN, Journal of Quantitative Spectroscopy and Radiative Transfer, 82, 491–504, https://doi.org/10.1016/S0022-4073(03)00173-0, 2003.

Paur, R. J. and Bass, A. M.: The Ultraviolet Cross-Sections of Ozone: II. Results and Temperature Dependence, in: Atmospheric Ozone, Springer, Dordrecht, 611–616, https://doi.org/10.1007/978-94-009-5313-0_121, 1985.

R, T. and R, V.: Temperature dependent absorption cross-sections of O2-O2 collision pairs between 340 and 630 nm and at atmospherically relevant pressure, Physical chemistry chemical physics : PCCP, 15, https://doi.org/10.1039/c3cp50968k, 2013.

Rodgers, C. D.: Inverse Methods for Atmospheric Sounding - Theory and Practice, https://doi.org/Inverse%20Methods%20for%20Atmospheric%20Sounding%20-%20Theory%20and%20Practice, 2000a.

Rodgers, C. D.: Inverse Methods for Atmospheric Sounding: Theory and Practice, https://doi.org/10.1142/3171, 2000b.

Rohrer, F., Bohn, B., Brauers, T., Brüning, D., Johnen, F.-J., Wahner, A., and Kleffmann, J.: Characterisation of the photolytic HONO-source in the atmosphere simulation chamber SAPHIR, Atmospheric Chemistry and Physics, 5, 2189–2201, https://doi.org/10.5194/acp-5-2189-2005, 2005.

Shetter, R., Stedman, D., and West, D.: The NO/NO2/O3 Photostationary State in Claremont, California, Journal of the Air Pollution Control Association, 1983.

Song, Y., Xing, C., Liu, C., Lin, J., Wu, H., Liu, T., Lin, H., Zhang, C., Tan, W., Ji, X., Liu, H., and Li, Q.: Evaluation of transport processes over North China Plain and Yangtze River Delta using MAX-DOAS observations, Atmospheric Chemistry and Physics, 23, 1803–1824, https://doi.org/10.5194/acp-23-1803-2023, 2023.

Vandaele, A. C., Hermans, C., Simon, P. C., Carleer, M., Colin, R., Fally, S., Mérienne, M. F., Jenouvrier, A., and Coquart, B.: Measurements of the NO2 absorption cross-section from 42 000 cm−1 to 10 000 cm−1 (238–1000 nm) at 220 K and 294 K, Journal of Quantitative Spectroscopy and Radiative Transfer, 59, 171–184, https://doi.org/10.1016/S0022-4073(97)00168-4, 1998.

Villena, G., Wiesen, P., Cantrell, C. A., Flocke, F., Fried, A., Hall, S. R., Hornbrook, R. S., Knapp, D., Kosciuch, E., Mauldin, R. L., McGrath, J. A., Montzka, D., Richter, D., Ullmann, K., Walega, J., Weibring, P., Weinheimer, A., Staebler, R. M., Liao, J., Huey, L. G., and Kleffmann, J.: Nitrous acid (HONO) during polar spring in Barrow, Alaska: A net source of OH radicals?, Journal of Geophysical Research, 116, https://doi.org/10.1029/2011JD016643, 2011.

Wagner, T., Remmers, J., Beirle, S., Ziegler, S., Shaiganfar, R., and Ziegler, M.: Characterisation of cloud properties from MAX-DOAS observations, 6306, 2013.

Wang, Y., Lampel, J., Xie, P., Beirle, S., Li, A., Wu, D., and Wagner, T.: Ground-based MAX-DOAS observations of tropospheric aerosols, NO_2, SO_2 and HCHO in Wuxi, China, from 2011 to 2014, Atmospheric Chemistry and Physics, 17, 2189–2215, https://doi.org/10.5194/acp-17-2189-2017, 2017.

Wang, Y., Apituley, A., Bais, A., Beirle, S., Benavent, N., Borovski, A., Bruchkouski, I., Chan, K. L., Donner, S., Drosoglou, T., Finkenzeller, H., Friedrich, M. M., Frieß, U., Garcia-Nieto, D., Gómez-Martín, L., Hendrick, F., Hilboll, A., Jin, J., Johnston, P., Koenig, T. K., Kreher, K., Kumar, V., Kyuberis, A., Lampel, J., Liu, C., Liu, H., Ma, J., Polyansky, O. L., Postylyakov, O., Querel, R., Saiz-Lopez, A., Schmitt, S., Tian, X., Tirpitz, J.-L., Van Roozendael, M., Volkamer, R., Wang, Z., Xie, P., Xing, C., Xu, J., Yela, M., Zhang, C., and Wagner, T.: Inter-comparison of MAX-DOAS measurements of tropospheric HONO slant column densities and vertical profiles during the CINDI-2 campaign, Atmospheric Measurement Techniques, 13, 5087–5116, https://doi.org/10.5194/amt-13-5087-2020, 2020.

Wentzell, J. J. B., Schiller, C. L., and Harris, G. W.: Measurements of HONO during BAQS-Met, Atmospheric Chemistry and Physics, 10, 12285–12293, https://doi.org/10.5194/acp-10-12285-2010, 2010.

Xing, C., Liu, C., Wang, S., Chan, K. L., Gao, Y., Huang, X., Su, W., Zhang, C., Dong, Y., Fan, G., Zhang, T., Chen, Z., Hu, Q., Su, H., Xie, Z., and Liu, J.: Observations of the vertical distributions of summertime atmospheric pollutants and the corresponding ozone production in Shanghai, China, Atmospheric Chemistry and Physics, 17, 14275–14289, https://doi.org/10.5194/acp-17-14275-2017, 2017.

Xing, C., Liu, C., Wang, S., Hu, Q., Liu, H., Tan, W., Zhang, W., Li, B., and Liu, J.: A new method to determine the aerosol optical properties from multiple-wavelength O_4 absorptions by MAX-DOAS observation, Atmospheric Measurement Techniques, 12, 3289–3302, https://doi.org/10.5194/amt-12-3289-2019, 2019.

Xing, C., Xu, S., Song, Y., Liu, C., Liu, Y., Lu, K., Tan, W., Zhang, C., Hu, Q., Wang, S., Wu, H., and Lin, H.: A new insight into the vertical differences in NO_2 heterogeneous reaction to produce HONO over inland and marginal seas, Atmospheric Chemistry and Physics, 23, 5815–5834, https://doi.org/10.5194/acp-23-5815-2023, 2023.

Xing, C., Liu, C., Li, Q., Wang, S., Tan, W., Zou, T., Wang, Z., and Lu, C.: Observations of HONO and its precursors between urban and its surrounding agricultural fields: The vertical transports, sources and contribution to OH, Science of The Total Environment, 915, 169159, https://doi.org/10.1016/j.scitotenv.2023.169159, 2024a.

Xing, C., Liu, C., Li, Q., Wang, S., Tan, W., Zou, T., Wang, Z., and Lu, C.: Observations of HONO and its precursors between urban and its surrounding agricultural fields: The vertical transports, sources and contribution to OH, Sci Total Environ, 915, 169159, https://doi.org/10.1016/j.scitotenv.2023.169159, 2024b.

Xing, C., Liu, C., Ye, C., Xue, J., Wu, H., Ji, X., Ou, J., and Hu, Q.: Observations of the vertical distributions of summertime atmospheric pollutants in Nam Co: OH production and source analysis, Atmospheric Chemistry and Physics, 24, 10093–10112, https://doi.org/10.5194/acp-24-10093-2024, 2024c.

Xue, C., Ye, C., Zhang, C., Catoire, V., Liu, P., Gu, R., Zhang, J., Ma, Z., Zhao, X., Zhang, W., Ren, Y., Krysztofiak, G., Tong, S., Xue, L., An, J., Ge, M., Mellouki, A. S., and Mu, Y.: Evidence for Strong HONO Emission from Fertilized Agricultural Fields and its Remarkable Impact on Regional O 3 Pollution in the Summer North China Plain, ACS Earth and Space Chemistry, 5, 340–347,

https://doi.org/10.1021/acsearthspacechem.0c00314, 2021.

Xue, C., Ye, C., Kleffmann, J., Zhang, C., Catoire, V., Bao, F., Mellouki, A., Xue, L., Chen, J., Lu, K., Zhao, Y., Liu, H., Guo, Z., and Mu, Y.: Atmospheric measurements at Mt. Tai – Part I: HONO formation and its role in the oxidizing capacity of the upper boundary layer, Atmospheric Chemistry and Physics, 22, 3149–3167, https://doi.org/10.5194/acp-22-3149-2022, 2022.

Zhang, S., Li, G., Ma, N., He, Y., Zhu, S., Pan, X., Dong, W., Zhang, Y., Luo, Q., Ditas, J., Kuhn, U., Zhang, Y., Yuan, B., Wang, Z., Cheng, P., Hong, J., Tao, J., Xu, W., Kuang, Y., Wang, Q., Sun, Y., Zhou, G., Cheng, Y., and Su, H.: Exploring HONO formation and its role in driving secondary pollutants formation during winter in the North China Plain, Journal of Environmental Sciences, 132, 83–97, https://doi.org/10.1016/j.jes.2022.09.034, 2023.

Zhou, X., Gao, X., Chang, Y., Zhao, S., and Li, Y.: Influence of atmospheric oxidation capacity on atmospheric particulate matters concentration in Lanzhou, Science of The Total Environment, 914, 169664, https://doi.org/10.1016/j.scitotenv.2023.169664, 2024.

Zou, T., Xing, C., Ji, X., Wei, S., Tan, W., Liu, H., and Liu, C.: A dataset of vertical profiles of O_3 and HONO from the hyperspectral vertical remote sensing network in China (2021–2024), Earth System Science Data, 18, 3559–3585, https://doi.org/10.5194/essd-18-3559-2026, 2026.